Finite-element modeling of subglacial cavities and related friction law

Olivier Gagliardini, D. Cohen, P. Raback, Thomas Zwinger

Correction published 21 November 2007

Finite-element modeling of subglacial cavities and related friction law

O. Gagliardini,[1] D. Cohen,[2] P. Råback,[3] and T. Zwinger[3]

Received 15 May 2006; revised 7 December 2006; accepted 25 January 2007; published 31 May 2007.

[1] Sliding velocity and basal drag are strongly influenced by changes in subglacial water pressure or subglacial water storage associated with opening and closing of water cavities in the lee of bedrock obstacles. To better understand this influence, finite-element simulations of ice flowing past bedrock obstacles with cavity formation are carried out for different synthetic periodic bedrock shapes. In the numerical model, the cavity roof is treated as an unknown free surface and is part of the solution. As an improvement over earlier studies, the cases of nonlinear ice rheology and infinite bedrock slopes are treated. Our results show that the relationship between basal drag and sliding velocity, the friction law, can be easily extended from linear to nonlinear ice rheology and is bounded even for bedrocks with locally infinite slopes. Combining our results with earlier works by others, a phenomenological friction law is proposed that includes three independent parameters that depend only on the bedrock geometry. This formulation yields an upper bound of the basal drag for finite sliding velocity and a decrease in the basal drag at low effective pressure or high velocity. This law should dramatically alter results of models of temperate glaciers and should also have important repercussions on models of glacier surges and fast glacier flows.

Citation: Gagliardini, O., D. Cohen, P. Råback, and T. Zwinger (2007), Finite-element modeling of subglacial cavities and related friction law, *J. Geophys. Res.*, *112*, F02027, doi:10.1029/2006JF000576.

1. Introduction

[2] Numerous field studies show that the sliding speed of temperate glaciers is strongly affected by daily and seasonal changes in water pressure or water storage [e.g., *Iken and Bindschadler*, 1987; *Hooke et al.*, 1989; *Iken and Truffer*, 1997; *Hanson et al.*, 1998; *Anderson et al.*, 2004]. Over the last 50 years, considerable efforts have been devoted to modeling basal sliding first without, and then with formation of water cavities [e.g., *Weertman*, 1957; *Lliboutry*, 1968, 1979; *Nye*, 1969, 1970; *Kamb*, 1970, 1987; *Morland*, 1984; *Fowler*, 1981, 1986, 1987; *Gudmundsson*, 1997a, 1997b; *Schoof*, 2005]. Making the assumption that ice is temperate and clean and thus slides without friction over a rigid bedrock, these studies aimed at determining the relationship between the mean basal drag induced by the bedrock roughness, the mean sliding velocity, and the effective pressure (the ice pressure minus the water pressure). This relationship, the friction law, can then be used as a (Robin-type) basal boundary condition on a smoothed bedrock surface for which small obstacles have been eliminated. The term ''friction'' law is used here to distinguish it from a sliding law where the sliding speed is expressed explicitly as a function of basal drag and effective pressure. Such explicit relation between velocity and basal drag allows the basal drag to be equated with the driving stress, leading to a (Dirichlet) velocity boundary condition at the bedrock boundary.

[3] With the assumption of negligible friction between ice and rock, basal resistance to shear is due entirely to viscous and regelation flow of ice past bedrock obstacles. As long as the sliding velocity or the water pressure is small, the ice is in contact with the bed everywhere. With increasing water pressure, water cavities form in the lee of bedrock obstacles where the normal stress experienced by ice is lower than the water pressure. The presence of water-filled cavities decreases the area of the bed in contact with the ice and consequently the friction law is modified.

[4] *Lliboutry* [1968] showed that, in the presence of cavitation, basal friction should decrease for increasing water pressure. He proposed that the friction law should include the basal drag τ_b, the sliding velocity u_b, and the effective pressure $N = p_i - p_w$, where p_i and p_w are the ice overburden pressure and the water pressure, respectively [*Lliboutry*, 1979]. *Iken* [1981] inferred from a simple force balance of ice sliding on a bed consisting of rectangular steps that the quantity τ_b/N satisfies an upper bound determined only by the maximum up-slope of the bed: $\tau_b/N \leq m_{\max}$. A proof of the existence of Iken's bound was achieved by *Schoof* [2005] for a general bed geometry only restricted to bounded slopes.

[1] Laboratoire de Glaciologie et Géophysique de l'Environnement, CNRS, UJF-Grenoble I, Saint-Martin d'Hères, France.
[2] Department of Geological and Atmospheric Sciences, Iowa State University, Ames, Iowa, USA.
[3] CSC-Scientific Computing Ltd., Espoo, Finland.

0148-0227/07/2006JF000576

[5] The empirical sliding law [*Paterson*, 1994]

$$u_b \sim \tau_b^p / N^q \quad p, q > 0\,, \tag{1}$$

is commonly used in models of temperate glaciers [e.g., *Bindschadler*, 1983; *Van der Veen*, 1987; *Pattyn*, 1996, 2002; *Le Meur and Vincent*, 2003]. It implies a basal drag that increases without bound with increasing sliding velocity or effective pressure. As cavities form in the lee of bedrock obstacles as a result of increasing water pressure, basal drag reaches a maximum value determined by the maximum up-slope of the bed [*Schoof*, 2005], invalidating equation (1).

[6] In the present paper, numerical simulations are carried out to derive a friction law for glacier flow in the presence of cavitation. Both the shape of cavities and the resulting friction law are obtained for periodic synthetic bedrock geometries. The ice is assumed to slide without friction over a rigid undulating bed. Regelation and melting are neglected (see section 2 for hypotheses and numerical methods). The effect of nonlinear ice rheology is studied (section 3). Using a bedrock composed of two inverted half-ellipsoids, the existence of *Iken*'s [1981] bound for infinite slopes is discussed (section 4). In section 5, numerical experiments are discussed and key results summarized. Finally, in section 7, we propose a phenomenological friction law with three geometrical parameters that reproduces the main features obtained from our numerical experiments with synthetic bedrock geometries.

2. Formulation of the Problem and Numerical Method

2.1. Main Assumptions

[7] The main assumptions of the finite element (FE) simulations are: (1) ice slides without friction over a rigid bedrock, (2) water pressure, p_w, is constant in space, (3) regelation and melting of ice are neglected, (4) temperature is constant in space, (5) gravity is neglected and the weight of ice above the modeled domain is replaced by an equivalent ice overburden pressure, and (6) inertia and acceleration are neglected in the Navier-Stokes equations.

2.2. Equations to be Solved

[8] The constitutive law for the ice behavior is given by a Norton-Hoff type law (Glen's flow law in glaciology)

$$S_{ij} = 2\eta D_{ij}\,, \tag{2}$$

where $\mathbf{S}$ is the deviatoric stress tensor, $D_{ij} = (u_{i,j} + u_{j,i})/2$ are the components of the strain-rate tensor, and $\mathbf{u}$ is the velocity. The effective viscosity η can be expressed as

$$\eta = B^{-1/n} \gamma_e^{(1-n)/n}\,, \tag{3}$$

where the strain-rate invariant γ_e is defined as

$$\gamma_e^2 = 2 D_{ij} D_{ij}\,. \tag{4}$$

In equation (3), the fluidity parameter B is a constant since ice is assumed isothermal.

[9] The equations to be solved are the stress-equilibrium equation

$$S_{ij,j} - p_{,i} = 0\,, \tag{5}$$

and the incompressibility equation

$$D_{ii} = u_{i,i} = 0\,. \tag{6}$$

Only applied stresses at boundaries are taken into account and the stress variation due to the force of gravity is neglected in equation (5).

[10] The elevation of the cavity roof $y = h(x)$ is part of the system of unknowns to be solved. The cavity roof is a free surface and, since both regelation and melting are neglected, the flow velocities are tangential to the cavity roof, i.e.,

$$u \frac{\partial h}{\partial x} - v = 0\,. \tag{7}$$

Since the elevation of the cavity cannot be less than the bedrock surface, the following topological condition must be fulfilled:

$$h(x) \geq b(x)\,, \tag{8}$$

where $y = b(x)$ is the equation of the bedrock geometry.

2.3. Boundary Conditions

[11] The domain is horizontally periodic of period λ corresponding to one wavelength. For the bottom boundary, the ice is either in contact with water or with the bedrock. This leads to two different types of boundary conditions: (1) the ice-bedrock condition $\mathbf{u} \cdot \mathbf{n} = 0$ applies if $h = b$ and $-\sigma_{nn} > p_w$; and (2) the ice-water condition $\sigma_{nn} = -p_w$ applies if $h > b$ or if $h = b$ and $-\sigma_{nn} \leq p_w$. Here $\mathbf{n}$ is the upward pointing normal unit vector to the bed-cavity boundary and $\sigma_{nn} = \mathbf{n} \cdot \boldsymbol{\sigma} \mathbf{n}$ is the local normal stress on the bed-cavity boundary.

[12] For the driving force, a natural choice is to model the entire height of the glacier subject to the force of gravity as done by *Gudmundsson* [1997b]. To speed computation, however, the height of ice should be reduced since bedrock perturbations on the ice flow decrease as the distance above the bed increases. Then, gravity can be replaced by uniform normal and tangential stresses applied on a fictitious boundary sufficiently far above the bed but well below the glacier free surface. Since we expect basal drag to be bounded when water cavities are present, such stress loading will become unstable for configurations where the applied shear stress is larger than the bound. Thus, with stress-driven tests, one can only obtain the first part of the friction law up to the bound. To obtain the full relationship between basal drag and sliding velocity past the maximum value of the basal drag, one needs to apply a velocity-driven boundary condition at the top of the domain. In what follows, the top of the domain, $y = H$, represents a fictitious boundary at which a horizontal velocity, $\bar{u}$, and a vertical normal stress, $\bar{p}_i$, representing the ice overburden pressure above the domain, are applied. These two quantities are assumed to be uniform over the top of the domain. The basal drag is then calculated afterward from the resulting velocity field as

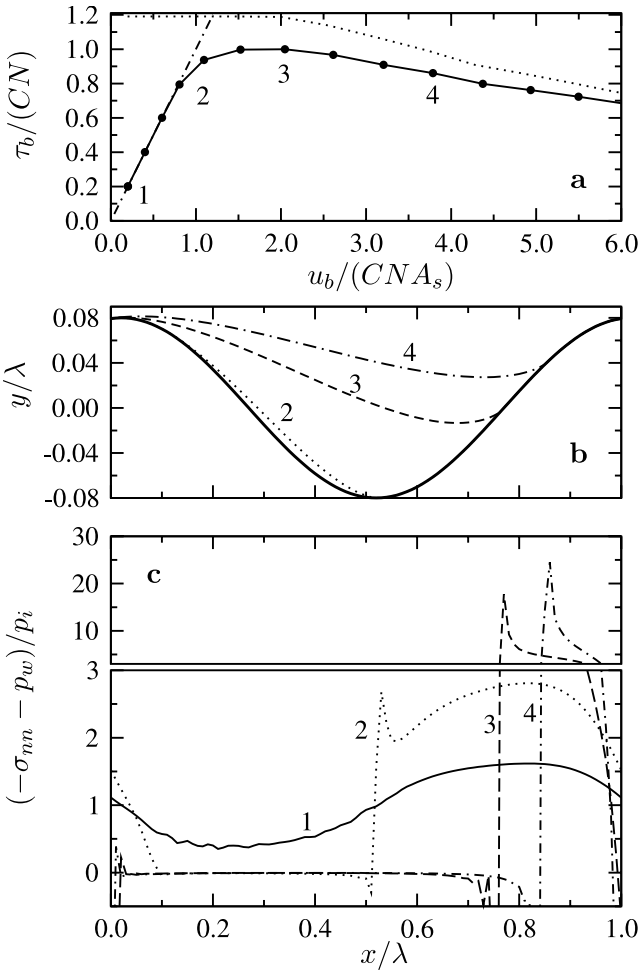

Figure 1. (a) Friction law calculated for a sinusoidal bedrock of roughness $r = 0.08$ and linear ice behavior (solid line). The dotted curve represents the maximum positive bedrock slope restricted to the area of ice-bed contact, $m_{\max}^{\text{contact}}$, normalized by the maximum value reached by $C = \max(\tau_b/N)$. The dash-dotted line corresponds to the friction law in the absence of cavitation $u_b = A_s \tau_b^n$. (b) Sinusoidal bed and cavity shapes and (c) normalized local effective pressure on the bed-cavity boundary for four different water-pressure levels labeled 1 through 4 in Figure 1a.

explained below. The influence of the fictitious boundary position, i.e., the domain height H, on the resulting friction law is discussed in section 3.4.

2.4. Numerical Methods

[13] The set of equations is solved using the open source FE code Elmer available at http://www.csc.fi/elmer. We hereafter only discuss the particular implementations needed for these simulations.

[14] Concerning the Stokes equations, the treatment of the bed-cavity boundary condition is done using a conditional Dirichlet boundary condition $\mathbf{u}.\mathbf{n} = 0$ which applies only at nodes where $h = b$ and $-\sigma_{nn} > p_w$. For other nodes, the Neumann condition $\sigma_{nn} = -p_w$ applies.

[15] Linear elements stabilized using the residual free bubbles method [*Baiocchi et al.*, 1993] or quadratic $P2P1$ elements (i.e., the classical quadratic velocity basis function and linear pressure basis function elements) were both tried, as well as structured and unstructured meshes. How element and mesh types influence numerical results is discussed later.

[16] The calculation of the stress from the velocity and isotropic pressure fields is a matter of interest because different methods can lead to detectably different solutions. In this study, the deviatoric stress field is obtained by solving equation (2) using the following variational form with the scalar test functions Φ:

$$\int_V S_{ij}\Phi \mathrm{d}V = 2\int_V \eta D_{ij}\Phi \mathrm{d}V \ , \tag{9}$$

where D_{ij} and η are calculated from the nodal velocities using the derivative of the basis functions. The bedrock inequality constraint (8) is implemented by adding a penalty term to the free surface variational form [*Donea and Huerta*, 2003].

2.5. Inferring the Friction Law

[17] For a given set of boundary conditions (i.e., water pressure p_w, overburden ice pressure $\bar{p}_i$, and horizontal velocity $\bar{u}$), the Stokes and free surface equations are solved iteratively until a steady state solution is reached. From the steady-state stress fields, the normal component of the stress, σ_{nn}, is evaluated on the bedrock-cavity surface. Using the FE interpolation function, the average basal drag is calculated as the moment over the boundary of the horizontal part of the normal stress, i.e.,

$$\tau_b = \frac{1}{\lambda}\int_0^\lambda \sigma_{nn} n_x \mathrm{d}s = -\frac{1}{\lambda}\int_0^\lambda \sigma_{nn}\frac{\partial h}{\partial x}\mathrm{d}x \, . \tag{10}$$

As a verification of the numerical method, the mean vertical contribution of σ_{nn} on the bottom boundary is calculated as

$$p_i = -\frac{1}{\lambda}\int_0^\lambda \sigma_{nn} n_y \mathrm{d}s = -\frac{1}{\lambda}\int_0^\lambda \sigma_{nn}\mathrm{d}x \tag{11}$$

and compared to the applied overburden ice pressure $\bar{p}_i$. In all solutions, the relative difference between p_i and $\bar{p}_i$ is less than 1%. The effective pressure is then calculated as $N = p_i - p_w$.

[18] From the steady state velocity field, the sliding velocity is calculated as the mean value of the horizontal component of the velocity u on the bedrock-cavity boundary:

$$u_b = \frac{1}{\lambda}\int_0^\lambda u \mathrm{d}x \, . \tag{12}$$

Owing to viscous resistance, the inequality $u_b < \bar{u}$ is always satisfied.

[19] This calculation is repeated for a new set of boundary conditions with different values of p_w, p_i, and $\bar{u}$. From a practical point of view, either the value of the water pressure, or the velocity, or the overburden ice pressure can be modified to get a new point that describes the friction law function. For a given geometry and ice rheology, this stage is repeated approximately twenty times in order to

Table 1. Comparison of $c_0(n)$ From Different Studies

n	1	2	3	4
Gudmundsson [1997b]	0.9936	0.5661	0.3294	0.1943
This study	0.9771	0.5140	0.2769	0.1515

obtain a smooth plot of basal drag as a function of sliding speed (Figure 1a).

3. Sinusoidal Bedrock and Nonlinear Behavior

[20] The special case of ice sliding without friction over a periodic sinusoidal bed in the presence of cavities has been treated using perturbation theory [*Lliboutry*, 1968; *Kamb*, 1987; *Fowler*, 1986; *Schoof*, 2005] and the FE method [*Iken*, 1981], but a linear ice rheology was assumed in all these studies. When presented, the nonlinear extension was always built from heuristic considerations [*Kamb*, 1987; *Fowler*, 1986, 1987]. In the following, we present the first results obtained for various power-law exponents ranging from $n = 1$ to $n = 4$.

3.1. Sliding in the Absence of Cavitation

[21] It has been shown through various approaches [*Lliboutry*, 1968, 1987; *Fowler*, 1981; *Gudmundsson*, 1997b] that, in the case of ice sliding without cavitation over an undulating bed, the resulting basal drag and mean sliding velocity verify the following relation:

$$u_b = A_s \tau_b^n , \tag{13}$$

where n is the exponent in Glen's flow law and A_s is the sliding parameter in the absence of cavitation. From dimensional analysis, *Lliboutry* [1987] and *Gudmundsson* [1997b] showed that $A_s \propto B\ \lambda$ and that A_s should only depend on three dimensionless parameters: the roughness $r = a/\lambda$, where a is the obstacle's amplitude, the thinness parameter $\delta = \lambda/(2\pi E)$, where E is the glacier thickness, and n. From results of a model for nonlinear ice behavior, *Fowler* [1981] demonstrated that $A_s \propto 1/r^{n+1}$. Note that *Gudmundsson* [1997b] translated this result into $A_s \propto 1/m_{\max}^{n+1}$, which is only true in the special case of a sinusoidal bed where $m_{\max} \propto 2\pi r$.

[22] From these results, one can write the sliding parameter in the absence of cavitation as

$$A_s = \frac{1}{(2\pi)^{n+2}} \frac{B\lambda}{r^{n+1}} s_G(r, \delta, n) , \tag{14}$$

where $s_G(r, \delta, n)$ is a dimensionless geometrical parameter that depends on the bedrock geometry and the exponent of Glen's flow law. From a numerical point of view, an accurate computation of the geometric parameter s_G also depends on the mesh resolution, as discussed in section 3.4. Note that equation (14) is only valid for small thinness value, i.e., for bedrock obstacle wavelengths that are small in comparison with the ice thickness [*Gudmundsson*, 1997b; *Schoof*, 2002].

[23] From linear perturbation theory, *Kamb* [1970] deduced that $\lim_{r\to 0} s_G(r, 0, 1) = 1$. Using FE modeling, *Gudmundsson* [1997b] estimated s_G as a Taylor series with respect to the maximum bedrock slope for $n = 1$ to $n = 5$, for $\lambda/E = 0.05$, and for roughnesses ranging from $r = 0.001$ to $r = 1.0$. In his approach, the mesh height H is equal to the glacier ice thickness E, the top boundary is a stress-free surface, and the flow is driven by gravity.

[24] In order to compare our estimates of the sliding parameter A_s with the results of *Gudmundsson* [1997b], s_G is reduced to a constant function, i.e., $s_G(r, \delta, n) = c_0(n)$, which corresponds to the constant term of the Taylor series used by *Gudmundsson* [1997b]. For $n = 1$ to $n = 4$, Table 1 gives the values of $c_0(n)$ for the two approaches. The relative difference between the two estimates of $c_0(n)$ varies from 1.6% for $n = 1$ to 22% for $n = 4$. Such large differences in the nonlinear cases arise because the problem is solved by two slightly different approaches: in our analysis, as discussed earlier, it is not possible to apply a gravitational driving force as was done by *Gudmundsson* [1997b]. The driving force is replaced by an equivalent overburden ice pressure and a horizontal ice velocity at the top of the numerical domain. It was not possible to ensure that the ratio of the shear stress relative to the ice overburden pressure was equivalent to the ratio used in the simulations done by *Gudmundsson* [1997b] for two reasons: first, the value of the mean surface slope is not given by *Gudmundsson* [1997b]; second, in our approach, a bed-parallel driven velocity is applied instead of a shear stress, for the reason explained in section 2.3. In the remainder of the paper, the sliding parameter A_s is calculated at the beginning of each tests and this value is used to plot the results.

3.2. Linear Behavior and Different Roughness

[25] The friction law obtained for a roughness $r = 0.08$ and a linear behavior is plotted in Figure 1a (solid line). As suggested by *Fowler* [1986], the friction law is plotted as

$$\frac{\tau_b}{CN} = f\left(\frac{u_b}{CNA_s}\right) , \tag{15}$$

where A_s is the sliding parameter without cavitation and C is the maximum value reached by τ_b/N. Figures 1b and 1c show the shape of the cavity roof and the normalized local effective pressure, respectively, corresponding to 4 specific points along the curve of the friction law. At low water pressure (Point 1), $-\sigma_{nn} > -p_w$ and there is no cavity. At Point 2, the normal stress reaches the water pressure in the lee face of the obstacle and a cavity appears. When the cavity extends past the maximum bed slope on the obstacle's stoss side, the basal drag starts decreasing (Points 3 and 4). Because of a reduced contact area between ice and bedrock, the normal stress concentrates just past the point where ice makes contact with the bed, and this stress concentration becomes larger as the cavity size increases (see Figure 1c). The peak in normal stress downstream of the contact point is in accord with stress singularities predicted by *Fowler* [1986] and *Schoof* [2005]. With the FE method, the value of the simulated normal stress peak is mesh-dependent so that its maximum value should be used with care. For the case shown in Figure 1c, the maximum value of the normal stress is up to 20 times the ice overburden pressure. Although the value of the normal stress near the contact point will increase with mesh refinement, the integral of the normal stress to estimate τ_b (10) will converge to a given value.

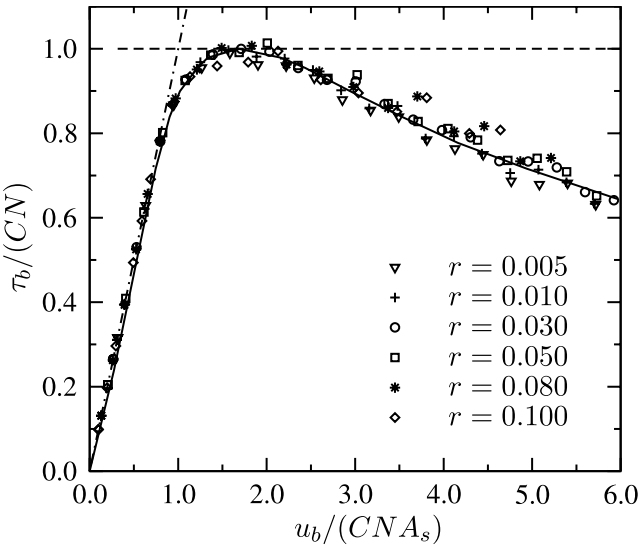

Figure 2. Friction law calculated for a sinusoidal bedrock and a linear ice rheology for different roughnesses ranging from $r = 0.005$ to $r = 0.1$. $C = 0.84\ m_{\max}$ was adopted to plot all curves. Very good agreement is found with the semianalytical result of *Schoof* [2005] (solid curve). The dash-dotted line corresponds to the friction law in the absence of cavitation $u_b = A_s {\tau_b}^n$ and the dashed line indicates the maximum value reached by $\tau_b/(CN)$.

[26] As shown in Figure 1a (dotted curve), the maximum positive bedrock slope restricted to the area of ice-bed contact, $m_{\max}^{\text{contact}}$, is always larger than τ_b/N. Using this new variable instead of the maximum bedrock slope, Iken's bound remains valid even after the maximum bedrock slope has been drowned by water in the cavity.

[27] To compare results with different roughnesses, the friction law for $n = 1$ for values of r ranging from 0.005 to 0.1 is shown in Figure 2. Within this range, all curves of the friction law can be superimposed on top of one another if using a friction law of the form (15), as predicted by *Fowler* [1986] using a scale analysis with linear rheology and small roughness. As a result, the maximum value of the friction law relative to the maximum slope, $C/m_{\max}$, is constant in the range of studied roughnesses. For all tests with linear rheology, $C/m_{\max} = 0.84 \pm 0.01$, which is in good agreement with *Fowler*'s [1986] and *Schoof*'s [2005] results.

[28] Moreover, the FE results perfectly superimpose with the friction law proposed by *Schoof* [2005], as shown in Figure 2. In work by *Schoof* [2005] the friction law is derived using dimensionless velocity ($\bar{u}_b$) and stress ($\tilde{\tau}_b$ and $\tilde{N}$), whereas we are using dimensional variables. The fact that the results superimpose indicates that the function f of Schoof ($\tilde{\tau}_b/\tilde{N} = f(\bar{u}_b/\tilde{N})$) and our function (15) are identical. As a consequence, dimensionless results of *Schoof* [2005] can be made dimensional by simply changing $\bar{u}_b/\tilde{N}$ to $u_b/(NA_s)$. Note that the parameter C in Figure 2, which appears in both axes, has no effect on the shape of the friction law for the linear case.

[29] Because the numerical method implemented for the free surface allows only vertical displacement of boundary nodes, the end point of the cavity is calculated with a precision that is of the same order as the distance between two consecutive nodes. As already shown by *Iken* [1981], a small error in the position of the end point can lead to a large error in the estimation of the basal drag. This large error is certainly, to a large extent, due to a poor estimate of the stress singularity at the contact point. The scatter of the FE results shown in Figure 2 can be attributed mostly to this error. The influence of mesh refinement on the resulting friction law is discussed in section 3.4.

3.3. Nonlinear Behavior

[30] Numerical tests for roughnesses $r = 0.05$ and $r = 0.08$ were performed for power-law exponents $n = 1$ to $n = 4$. As shown in Figure 3, all the resulting friction laws can be, more or less, superimposed if $[\tau_b/(CN)]^n$ is expressed as a function of $u_b/(C^n N^n A_s)$. For these tests, the maximum value of the friction law is $C/m_{\max} = 0.84 \pm 0.02$. Note that the sensitivity of the friction law to C increases with n. As discussed earlier, the error in the location of the node where the cavity reconnects to the bedrock explains the discrepancy between the results. The sensitivity of the position of that node increases with increasing values of n.

[31] Our results show the following. (1) The maximum value of τ_b/N does not depend on the power-law exponent n; that is, $C(n)$ is constant for a given bed geometry. (2) The friction law f is not modified by a change of n if the law is expressed in the form $[\tau_b/(CN)]^n = f(u_b/(C^n N^n A_s))$, as long as $A_s = A_s(n)$ takes the appropriate value.

[32] An important implication of these results is that the friction law for nonlinear ice rheology can be easily extrapolated from the linear case. Only the sliding parameter, $A_s(n)$, must be calculated as a function of n. Note that determining $A_s(n)$ is a simple problem in comparison to obtaining the full curve f of the friction law. Using the FE

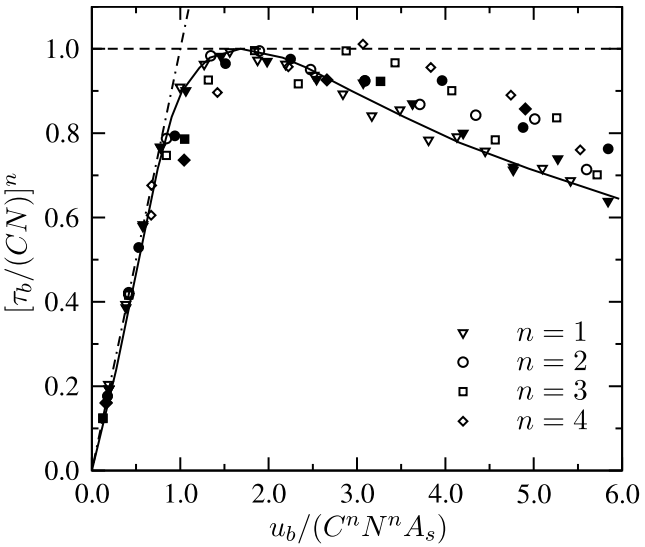

Figure 3. Friction law calculated for a sinusoidal bedrock for $n = 1$, 2, 3 and 4 for roughnesses $r = 0.05$ (open symbol) and $r = 0.08$ (solid symbol). $C = 0.84 \pm 0.02 \times m_{\max}$ was adopted to plot all results. The solid line shows the semianalytical friction law obtained by *Schoof* [2005] in the case of a linear rheology. Same definition for dashed and dash-dotted lines as in Figure 2.

Table 2. Characteristic of the Three Different Sinusoidal-Bed Meshes

Mesh	S1	S2	S3
Number of nodes	441	1581	4141
Number of B. nodes[a]	21	51	101
$\Delta m_{\mathrm{maxMesh}}$,[b] %	2.42	0.46	10^{-8}
$A_s/(B\lambda)$	0.5994	0.5930	0.5947
CPU[c]	1	4.2	13.3

[a]Number of nodes on the bedrock-cavity boundary.
[b]$\Delta m_{\mathrm{maxMesh}} = (m_{\mathrm{maxMesh}} - 2\pi r)/2\pi r$.
[c]Relative to mesh S1.

method, $A_s(n)$ can be obtained even for a complicated bedrock topography.

3.4. Influence of Mesh Characteristics

[33] In the present study, numerical results may be influenced by the following mesh characteristics: mesh refinement and mesh height. The former concerns any modeling done using the FE technique. The latter is inherent to our approach: instead of solving the entire ice thickness above the bedrock (as done for example by *Gudmundsson* [1997a]), our domain is truncated some distance away from the bed and a velocity and ice overburden pressure are applied there. Section 3.4.1 presents quantitative results to estimate the effects of mesh refinement on the friction law. In section 3.4.2 we show that our FE results are independent of the mesh height H if the height is large enough relative to the horizontal wavelength of the obstacle.

3.4.1. Mesh Refinement

[34] The influence of mesh refinement on FE results is tested by comparing the friction law obtained for the three different meshes described in Table 2. For these tests, $r = 0.08$ and $n = 1$. Structured, linear, quadrilateral elements are used. As shown in Table 2, the influence of mesh refinement on the sliding parameter A_s is small (less than 1%). Mesh refinement also has a small effect on the maximum value of τ_b/N, as shown in Figure 4. Thus the three meshes lead to nearly identical friction laws up to the peak in basal drag. After the peak, the friction law is more sensitive to mesh refinement. In Figure 4, the influence of the distance between two consecutive mesh nodes clearly affects the friction law. The curve for the coarser mesh (S1, 21 nodes along the bed) oscillates around the two other curves obtained with finer meshes (S2 and S3 with respectively 51 and 101 nodes along the bed) and these oscillations increase with cavity size (increasing u_b/N). These oscillations are due to the geometrical mismatch between the true contact point and the mesh node that represents the modeled contact point. When the true contact point and the node lie on top of each other, the estimate of the friction law for the coarse mesh is close to estimates with finer meshes. When the true contact point lies about equal distance between two consecutive mesh nodes, the estimate of friction is poor. The amplitude of oscillations for the coarse mesh probably increases with cavity size because normal stresses become large (see Figure 1c) and are less accurately estimated. In view of these results, all FE tests done in the remaining of this study were done using at least 51 nodes to describe the bedrock-cavity boundary.

3.4.2. Mesh Height

[35] As shown by *Gudmundsson* [1997b], the sliding parameter A_s depends on the ratio of the wavelength λ to the total glacier height E. Since in our approach gravity is neglected, the domain height H should be kept to a small value to reduce computing time. The perturbation on the velocity and stress fields induced by the bedrock obstacle is a decreasing function of the height above the bed. At some elevation, this perturbation becomes negligible and the different fields are constants along the horizontal direction. Therefore one can find a minimum height for which the constant boundary conditions applied at the top of the domain will negligibly influence the final results. This minimal mesh height is, of course, dependent on the bedrock roughness. Various meshes with H/λ ranging from 0.2 to 2.0 were tested showing that, as long as the mesh height is greater than $H = 0.5\lambda$, the friction law does not depend on mesh height.

4. Ellipsoidal Bedrock and Infinite Slope

[36] All analytical models of cavitation developed so far are limited by the assumption of bounded bedrock slopes. In the case of a bed with an infinite bed slope, a concentration of normal stress near the zone of infinite slope could generate increasingly large resistive forces, and hence an unbounded basal drag. This could only occur if the cavity does not extend past the maximum slope of the bedrock. If, on the contrary, the cavity extends past the point of maximum slope, the basal drag should not increase with increasing sliding speed, and one should observe a decreasing drag with sliding speed as in the case with bounded slopes. These two possible scenarios leave open the question of the existence of *Iken*'s [1981] bound in the case of an infinite slope.

[37] In the following calculations we try to answer this question. To this end, we study the flow of ice over an ellipsoidal bed characterized by a roughness $r = a/\lambda$, where a is the half length of the ellipsoid axis perpendicular to the mean direction of the flow. The bed is periodic of wavelength λ and within the period is composed of two inverted

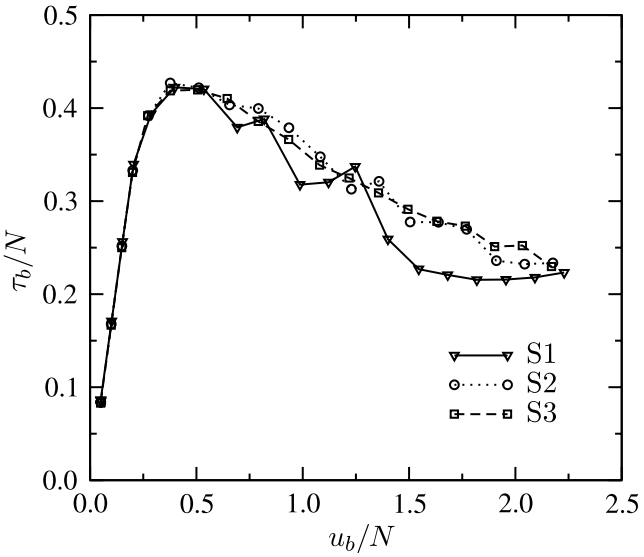

Figure 4. Influence of mesh refinement on the friction law for three different meshes defined in Table 2. Results are for a sinusoidal bedrock with $r = 0.08$ and $n = 1$.

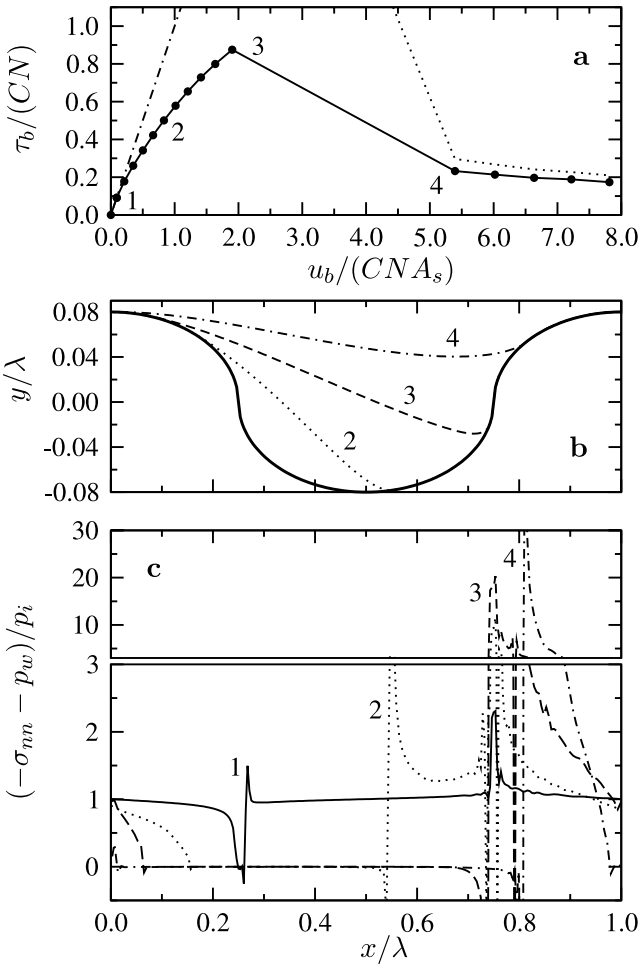

Figure 5. (a) Friction law calculated for the ellipsoidal bedrock of roughness $r = 0.08$ and a linear ice behavior (solid curve). The dotted curve represents the maximum positive bedrock slope restricted to the area of ice-bed contact, $m_{\max}^{\text{contact}}$, over C. The dash-dotted line corresponds to the friction law in the absence of cavitation. (b) Ellipsoidal bed and cavity shapes, and (c) normalized local effective pressure on the bed-cavity boundary for four different water-pressure levels labeled 1 to 4 in Figure 5a.

half ellipsoids as shown in Figure 5b. At the junction of the two half ellipsoids the slope is theoretically infinite. For all these tests, the ice is taken to have a linear rheology ($n = 1$).

[38] As shown in Figure 5a, the friction law for an ellipsoidal bed is slightly different from that obtained for a sinusoidal bed. First, because of the large negative slope in the lee face of the ellipsoid, the normalized effective pressure is null there and a cavity exists even at low water pressures (Point 1). Second, there is a zone in the vicinity of the maximum bedrock slope where the cavity ends that is very unstable (note that Points 3 and 4 are separated by the same increase in water pressure than any other two points in the friction law curve shown in Figure 5a). Two interpretations of the curve in Figure 5a are possible: either there are some missing points on the curve between Points 3 and 4 which would show the basal drag increasing without bound after Point 3, or the cavity is not stable when its end point

Table 3. Characteristic of the Four Different Ellipsoidal-Bed Meshes

Mesh	E1	E2	E3	E4
Element type	T3	T6	T6	Q4
Mesh type[a]	U	U	U	S
Number of nodes	1021	2092	3664	5226
Number of B. nodes[b]	97	97	129	201
m_{maxMesh}	5.0	1600	3800	2.4
$A_s/(B\lambda)$	0.247	0.267	0.216	0.284

[a]Unstructured or structured.
[b]Number of nodes on the bedrock-cavity boundary.

lies in the vicinity of the maximum bedrock slope. The following two tests attempt to answer this issue.

4.1. Influence of Mesh Refinement

[39] Several meshes were built such that one node would always fall exactly at the junction between two half ellipsoids. The slope at this node is strongly mesh-dependent and is never infinite. Comparison of results for the same bedrock geometry but with different levels of mesh refinements should be a good indicator of the influence of the value of the maximum slope on the friction law.

[40] We compare the results obtained for a bedrock roughness $r = 0.08$ using four meshes described in Table 3, with maximum mesh slopes that vary between 2.4 and 3800. Note the large difference in the maximum slope value between linear and quadratic boundary elements.

[41] A relative difference of about 15% is found between the computed sliding parameter A_s for the four meshes (see Table 3). This difference is large in comparison to the 1% difference obtained for the case of a sinusoidal bedrock. However, despite the large difference in A_s, all friction laws calculated with the four meshes are very close, as shown in Figure 6. The peak value of the friction law $C \approx 1.2$ does not depend on the value of the maximum mesh slope. Note

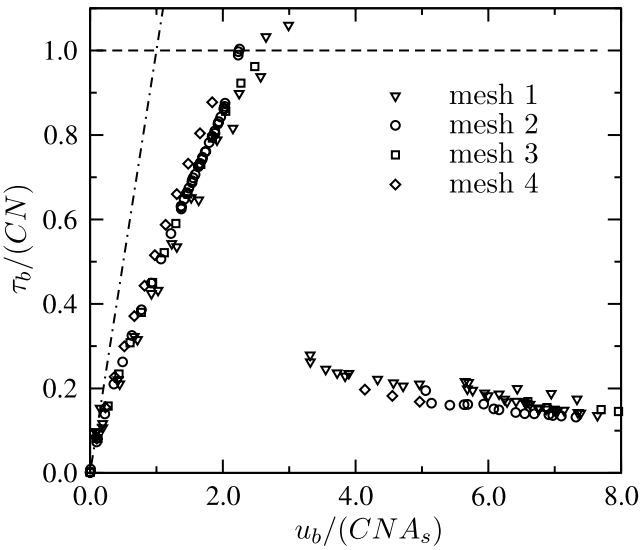

Figure 6. Friction law calculated for the ellipsoidal bedrock of roughness $r = 0.05$ for the four different meshes described in Table 3. $C = 1.2$ was adopted to plot all these curves. Same definition for dashed and dash-dotted lines as in Figure 2.

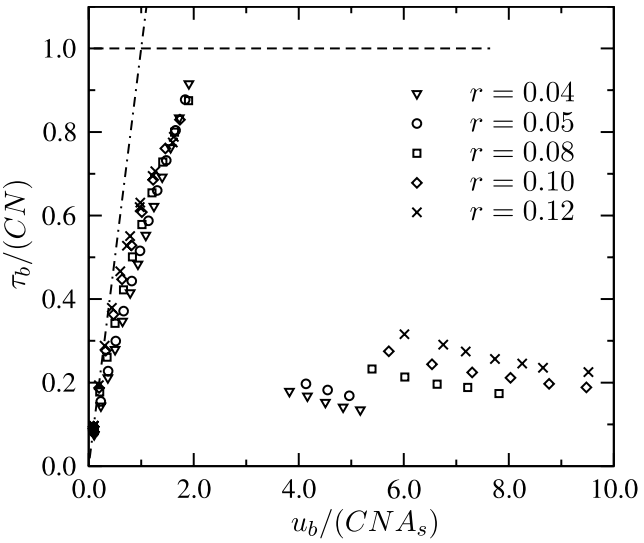

Figure 7. Friction law calculated for the ellipsoidal bedrock for different roughnesses ranging from $r = 0.04$ to $r = 0.12$. $C = 1.2$ was adopted to plot all the curves. Same definition applies for dashed and dash-dotted lines as given in Figure 2.

that it was not possible to add points in the region of the discontinuity even by decreasing the interval of the water pressure between two steady state solutions. From this result, one can conclude that the resulting sliding law for the ellipsoidal bedrock does not depend on the actual maximum mesh slope.

4.2. Different Roughnesses

[42] To confirm this result, the friction law is calculated for roughnesses ranging from $r = 0.04$ to $r = 0.12$. In all these tests, the mesh has the same number of elements and nodes, resulting in the value of the maximum mesh slope to be proportional to the roughness. Results from these tests indicate that the sliding parameter can be estimated as

$$A_s = B\lambda \frac{-2 \times 10^{-5} + 0.013r + 0.0262r^2}{r^2}\,, \tag{16}$$

with a root-mean-square error less than 0.03%.

[43] According to Figure 7, the peak value of the friction law $C \approx 1.2$ does not depend on the roughness, but the postpeak decrease does. If one replaces C by the roughness r in Figure 7, the postpeak curves can be superimposed (then, of course, the prepeak curves no longer superimpose). It was not possible to superimpose the complete friction curves for the ellipsoidal bedrock on one single curve. As in the case of the sinusoidal bedrock, the postpeak portion of the friction law is constrained by the maximum positive bedrock slope restricted to the area of ice-bed contact, $m_{\max}^{\text{contact}}$, as shown in Figure 5a (dotted curve). The abrupt change of the slope around the point of maximum slope explains the fast decrease of τ_b/N after this point has been overtaken by the water cavity. In the case of different roughnesses, as shown in Figure 7, the prepeak is not controlled by the roughness because, in all cases, the maximum slope $m_{\max}$, even if proportional to r, is very large. However, just after the point of maximum slope is overtaken by the cavity, $m_{\max}^{\text{contact}}$ quickly becomes much smaller, but is still proportional to r. The postpeak friction law is then controlled by the actual maximum slope $m_{\max}^{\text{contact}}$, explaining why the postpeak curves do not superimposed. Note that we have verified that each postpeak curve computed in this study is bounded by $m_{\max}^{\text{contact}}/C$ of the corresponding bedrock roughness. Although not a proof, results from Figures 6 and 7 show that the friction law remains bounded in the limiting case of an infinite bedrock slope.

5. Discussion of FE Results

[44] To characterize the peak and postpeak features of our periodic tests, we introduce the parameter $\Delta_m = m_{\max}/\bar{m}$, where $\bar{m} \sim 4\ r = 4\ a/\lambda$ is the mean positive bedrock slope calculated over the stoss face of the obstacle. The slope severity index, Δ_m, indicates how abrupt the slope is for a given roughness r.

[45] Using this parameter, it appears that Iken's bound seems to be less and less relevant as the slope severity index becomes larger, i.e., $C/m_{\max}$ decreases with increasing Δ_m. In other words, for large slope severity index, the upper limit on drag is a lot less than that predicted by Iken's bound. For a sawtooth bedrock (tests done by the authors but not presented here), $C = m_{\max}$ and $\Delta_m = 1$, while for the ellipsoid bedrock Δ_m is infinite and C is constant and does not depend on roughness. These two examples can be viewed as two end-member cases. For the sinusoidal bedrock, $C = 0.84m_{\max}$ and $\Delta_m = \pi/2$. Note that $C = m_{\max}$ for the sawtooth bedrock can be obtained analytically [C. Schoof, personal communication, 2006]. For large slope severity index, it becomes more and more difficult to reach the bound because the point of maximum slope is overtaken quickly by the cavity and then annihilated.

[46] The general pattern of the postpeak curve of our tests can also be characterized by the slope severity index Δ_m. The postpeak basal drag decrease is faster for larger Δ_m because larger Δ_m implies a large reduction of $m_{\max}^{\text{contact}}$ once the maximum slope has been overtaken by the cavity.

[47] Note that the above analysis using Δ_m applies to the case of periodic beds. Its application to nonperiodic beds is not straightforward.

6. General Conditions for a Sliding Law

[48] From our results obtained on periodic synthetic bedrocks and from works by others on more general bed topographies [*Fowler*, 1987; *Schoof*, 2005], some general conditions must be fulfilled by the friction law.

[49] 1. According to our results for the sinusoidal bed and the nonlinear rheology, an appropriate expression for this law is a function of the form

$$\left(\frac{\tau_b}{CN}\right)^n = f(\chi)\,, \tag{17}$$

where

$$\chi = \frac{u_b}{C^n N^n A_s}\,. \tag{18}$$

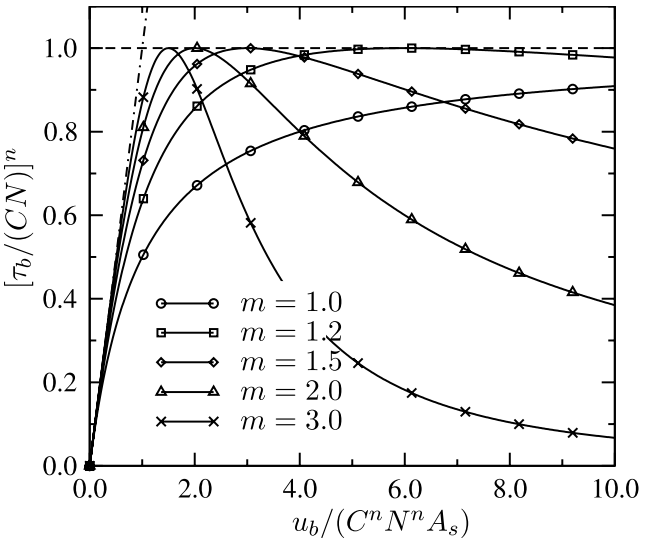

Figure 8. Proposed phenomenological friction law for different values of the parameter exponent q. Using these axes definition, the shape of the curves is not modified by a change in the two other parameters C and A_s. Same definition applies for dashed and dash-dotted lines as given in Figure 2.

An important aspect of the function f should be that it is independent of the power-law exponent n if one chooses the appropriate value for the sliding parameter, A_s, for each value of n. With this property results obtained in the linear case can be easily extended to nonlinear rheology. The heuristic assumption made by *Schoof* [2005] that τ_b/N is a function of u_b/N^n is then confirmed by our results.

[50] 2. For low water pressure, the friction law is tangential to the straight line obtained in the case of no cavitation, which can be written as

$$\left.\frac{\partial f}{\partial \chi}\right|_{\chi=0} = 1\,. \tag{19}$$

[51] 3. Here τ_b/N should reach a global maximum value $C \leq m_{\max}$ which is independent of the power-law exponent n:

$$\frac{\partial f}{\partial \chi} = 0 \Rightarrow f(\chi) = 1 \quad \forall n\,. \tag{20}$$

[52] 4. For higher water pressure, after the global maximum stress is reached at $\chi = \chi_M$, the friction law should decrease for χ larger than χ_M and τ_b/N should remain bounded by the maximum bedrock slope restricted to the area of ice-bed contact, $m_{\max}^{\text{contact}}$:

$$\frac{\tau_b}{N} \leq m_{\max}^{\text{contact}}\,. \tag{21}$$

This latest condition can be seen as the local extension of Iken's bound to the actual cavity configuration. Because, in general, the area of the ice-bed contact is not known a priori, condition (21) cannot be used to constrain point by point the postpeak friction law curve.

[53] The four conditions can be seen as general conditions to be fulfilled by a sliding law. These four conditions obtained from our numerical results on synthetic periodic bedrock and also (linear expression of the first but not the fourth condition) from works by other on more general bed geometries [*Fowler*, 1987; *Schoof*, 2005], should hold even for more complicated bedrock geometries. As demonstrated by *Schoof* [2005], the tail-off of a realistic bed composed of many different superimposed obstacle sizes and shapes may be suppressed significantly, so that, on the basis of our results, no more than (21) can be said regarding the postpeak behavior of the friction law for a real bedrock.

7. A Friction Law for Glacier Modeling

[54] We now follow the idea of *Schoof* [2005] who proposed a phenomenological friction law simple enough to be implemented in a glacier flow model. Our objective is not to propose a friction law that reproduces exactly our numerical results, but to give a formulation that captures the main features of sliding with cavitation, as enounced by the four previous general conditions. A possible parameterized form for the friction law that fulfills these conditions can be written as

$$\frac{\tau_b}{N} = C\left(\frac{\chi}{1+\alpha\chi^q}\right)^{1/n}, \tag{22}$$

where χ is given by (18) and the coefficient α is chosen so that condition (20) is fulfilled for all q,

$$\alpha = \frac{(q-1)^{q-1}}{q^q}\,. \tag{23}$$

[55] The peak value of the sliding law is obtained at $\chi_M = q/(q-1)$ which corresponds to the sliding velocity

$$u_b = \frac{q}{q-1} A_s C^n N^n\,. \tag{24}$$

In the limiting case where $q = 1$, the proposed friction law (22) is equivalent to the one proposed by *Schoof* [2005]. Schoof, however, predicted that τ_b/N is a function of u_b/N^n and not a function of $u_b/(C^n N^n)$.

[56] In addition to ice rheological parameters n and B, only three geometrical parameters (A_s, C, and q) enter in the phenomenological friction law (22). What values of A_s, C, and q should be used for a real bedrock? The sliding parameter, A_s, relates u_b and τ_b^n before cavitation occurs. Given a known bedrock profile and ice rheology, A_s can be estimated from FE simulations.

[57] The maximum value of τ_b/N in the friction law, C, is a positive value less than the bedrock maximum slope $m_{\max}$. Importantly, C is a constant for a given bedrock geometry, independent of Glen's flow law exponent, n. Our results indicate that the ratio $C/m_{\max}$ is a decreasing function of the *slope severity* Δ_m.

[58] The exponent parameter, q, controls the postpeak decrease of the friction law (Figure 8). The larger q is, the faster the friction law tends to zero after the peak. Note that, as shown by *Schoof* [2005], the postpeak form of the friction law is not necessarily a monotonically decreasing function, as in the case of a bedrock consisting of a

superposition of obstacles with many different wavelengths. This condition is assumed here for simplicity, but it is not a general feature of a friction law. Our tests show that q is an increasing function of Δ_m. For the sawtooth bedrock, basal drag increases asymptotically toward a maximum and q = 1.0 is an appropriate value for this geometry. For the ellipsoidal bedrock, $q \approx 3.0$ approximately reproduces the numerical simulations, whereas $q \approx 2.0$ should be used for the sinusoidal bedrock. If q = 1.0, there is no peak and the basal drag tends asymptotically to the maximum value $\tau_b/N = C$. This particular case should not be dismissed as it may yield more stable numerical solutions for models of glacier flow than a multivalued friction law when $q > 1$.

[59] From a practical point of view, a method to determine the three parameters C, q, and A_s for a real bedrock topography would be to couple two approaches: (1) use perturbation models with linear rheology, as done by *Schoof* [2005], to determine the corresponding friction law, f, and then estimate the optimal value of C and q that best fit f; and (2) use a FE model of the real bedrock without cavities to calculate A_s as a function of n.

[60] Determination of the friction law for a real bedrock would require precise knowledge of the bedrock profile at the decimeter to tens of meter scale. This information is usually not available. A few authors [*Benoist*, 1979; *Echelmeyer and Wang*, 1987; *Cuffey et al.*, 1999; *Hubbard et al.*, 2000] have measured bedrock profiles but only *Benoist* [1979] and *Hubbard et al.* [2000] made measurements at the scale of interest here. All these authors computed the spectral roughness of subglacial beds which links the density of bumps to their wave numbers. The spectral roughness by itself, however, is not sufficient to estimate all of the parameters in the friction law because some parameters in the law depend on the maximum slope of bedrock obstacles, a piece of information not provided in the spectral roughness. Ideally, in locations where a sufficiently large area of the bed can be precisely mapped (i.e., recently deglaciated glacier bedrock), FE calculations such as done here in combination with analytical methods could be used to estimate the three geometrical parameters. With the assumption that the roughness measured in the forefield of the glacier is representative of the roughness over ice-covered bedrock, the values of these three parameters could be used on a smoothed bedrock profile over the entire length of the glacier.

[61] Because the proposed phenomenological friction law is multivalued in the sliding speed and exhibits a maximum in the value of the basal drag, it cannot be used in combination with the shallow ice approximation (SIA) model [*Hutter*, 1983]. In SIA, basal drag is equated to the driving stress which may exceed the maximum basal drag given by the friction law. This problem does not arise with the unbounded sliding law given by equation (1). For example, both *Le Meur and Vincent* [2003] and *Pattyn* [1996] use equation (1) as a sliding law but *Le Meur and Vincent* [2003], using SIA, equated τ_b to the driving stress ($\rho\ g\ E\ \sin\alpha$, where ρ is ice density, g is gravity, E is ice thickness, and α is surface slope), whereas *Pattyn* [1996] uses τ_b as an unknown in his basal boundary condition to determine the sliding speed. Both options are possible with an unbounded sliding law of the form of equation (1). The approach of *Le Meur and Vincent* [2003] is no longer possible with the present friction law.

[62] Because the proposed friction law depends on the effective pressure N, a model of the subglacial hydraulic system will be needed. An estimate of the spatial variation of the water pressure at the base can be obtained by a simple parameterized model as in work by *Pattyn* [1996] or by coupling the ice-flow model with a more complex model for the glacier hydrology as proposed by *Flowers and Clarke* [2002a, 2002b]. As effective pressure will vary along the glacier bed and in time, the basal drag computed from the friction law will not be uniform or constant. This will allow such processes as stress redistribution to take place over the glacier bed as has been observed in field studies [e.g., *Raymond*, 1971; *Kavanaugh and Clarke*, 2001].

8. Conclusions

[63] The existence of water-filled cavity is ubiquitous in temperate ice sliding over hard bedrock and water cavities may also be present between ice and soft sediment layers. In this work, we show that the form of the friction law for linear ice rheology can be easily extended to nonlinear rheology. We also show that Iken's bound still holds in the case of an infinite bedrock slope. Moreover, a modified Iken's bound, which uses the maximum slope of the bedrock restricted to the area of ice-bed contact, constrains the value of the basal drag past its maximum value. These conditions, derived for a periodic bedrock, should hold for more general bed forms.

[64] From results obtained for synthetic periodic bedrocks, we propose a phenomenological friction law (equation 22) that should be used as an alternative to the commonly used sliding law $u_b = A_s \tau_b^p / N^q$ which fails to predict bounded basal drag. Identification of the three geometrical parameters of the proposed parameterized friction law will require a modeling effort using the strategy presented above that combines both analytical derivation of a friction law (for example using *Schoof*'s [2005] method) and our numerical model. This will yield a friction law for specific sites where bedrock roughness is known.

[65] As demonstrated here and by others [*Lliboutry*, 1979; *Fowler*, 1986; *Schoof*, 2005], bedrock geometry has a strong influence on the behavior of the friction law and thus an accurate description of the bedrock roughness at the decimeter to meter scale is necessary to make useful predictions of sliding speed in models of glacier flow. Additional mapping efforts would be useful to constrain the sensibility of the friction law parameters to various real glacier beds. For a given basal drag the sliding speed in our friction law is multivalued suggesting that this law could find some applications in glacier surges and fast glacier flows.

Notation

a	half height of obstacle, m.
A_s	sliding parameter without cavity, m Pa^{-n} a^{-1}.
b	bedrock elevation, m.
B	fluidity parameter, Pa^{-n} a^{-1}.
C	friction law maximum value $C \leq m_{\max}$.
$\mathbf{D}$	strain-rate tensor, a^{-1}.

E glacier thickness, m.
h cavity roof elevation, m.
H mesh height, m.
$m_{\max}$ maximum bedrock slope.
$m_{\max}^{\text{contact}}$ maximum bedrock slope restricted to the area of ice-bed contact.
$\bar{m}$ mean positive bedrock slope.
n power-law exponent.
$\mathbf{n}$ normal upward pointing normal vector to the bed-cavity boundary.
N effective pressure $N = p_i - p_w$, Pa.
p pressure (compressive-positive), Pa.
$\bar{p}_i$ applied overburden ice pressure, Pa.
p_i integrated ice pressure, Pa.
p_w water pressure, Pa.
q friction law exponent $q \geq 1$.
r bedrock roughness $r = a/\lambda$.
$\mathbf{S}$ deviatoric stress tensor, Pa.
u local horizontal velocity, m a^{-1}.
u_b mean sliding velocity, m a^{-1}.
v local vertical velocity, m a^{-1}.
x horizontal coordinate in flow direction, m.
y vertical coordinate, m.
γ_e invariant of the strain rate, a^{-1}.
δ thinness parameter $\delta = \lambda/(2\pi E)$.
Δ_m slope severity index $\Delta_m = m_{\max}/\bar{m}$.
η effective viscosity, Pa a.
σ Cauchy stress tensor (compressive-negative), Pa.
τ_b mean basal drag, Pa.

[66] **Acknowledgments.** We warmly thank C. Schoof and R. Hindmarsh for their constructive and helpful reviews, as well as the Associate Editor and R. Anderson (Editor). We thank C. Schoof for a discussion during the EGU 2006 General Assembly that improved the quality of the present paper. This work was done when O. Gagliardini was a Scientific Visitor at CSC, partly supported by the AFFRST and the Vilho, Yrjö, and Kalle Väisälä Foundation of the Finnish Academy. O. Gagliardini was funded by the French ANR project MIDIGA. D. Cohen was funded by the U.S. National Science Foundation grant EAR-0229692.

References

Anderson, R. S., S. P. Anderson, K. R. MacGregor, E. D. Waddington, S. O'Neel, C. A. Riihimaki, and M. G. Loso (2004), Strong feedbacks between hydrology and sliding of a small alpine glacier, *J. Geophys. Res.*, *109*, F03005, doi:10.1029/2004JF000120.

Baiocchi, C., F. Brezzi, and L. P. Franca (1993), Virtual bubbles and the Galerkin least squares method, *Comput. Methods Appl. Mech. Eng.*, *105*, 125–141.

Benoist, J.-P. (1979), The spectral power density and shadowing function of a glacial microrelief at the decimeter scale, *J. Glaciol.*, *23*, 57–66.

Bindschadler, R. (1983), The importance of pressurized subglacial water in separation and sliding at the glacier bed, *J. Glaciol.*, *29*, 3–19.

Cuffey, K. M., H. Conway, B. Hallet, A. M. Gades, and C. F. Raymond (1999), Interfacial water in polar glaciers and glacier sliding at −17°C, *Geophys. Res. Lett.*, *26*, 751–754.

Donea, J., and A. Huerta (2003), *Finite Element Methods for Flow Problems*, John Wiley, Hoboken, N. J.

Echelmeyer, K., and Z. Wang (1987), Direct observation of basal sliding and deformation of basal drift at sub-freezing temperatures, *J. Glaciol.*, *33*, 83–98.

Flowers, G. E., and G. K. C. Clarke (2002a), A multicomponent coupled model of glacier hydrology: 1. Theory and synthetic examples, *J. Geophys. Res.*, *107*(B11), 2287, doi:10.1029/2001JB001122.

Flowers, G. E., and G. K. C. Clarke (2002b), A multicomponent coupled model of glacier hydrology: 2. Application to Trapridge glacier, Yukon, Canada, *J. Geophys. Res.*, *107*(B11), 2288, doi:10.1029/2001JB001124.

Fowler, A. C. (1981), A theoretical treatment of the sliding of glaciers in the absence of cavitation, *Philos. Trans. R. Soc., Ser. A*, *298*, 637–685.

Fowler, A. C. (1986), A sliding law for glaciers of constant viscosity in the presence of subglacial cavitation, *Proc. R. Soc., Ser. A*, *407*, 147–170.

Fowler, A. C. (1987), Sliding with cavity formation, *J. Glaciol.*, *33*, 255–267.

Gudmundsson, G. H. (1997a), Basal-flow characteristics of a linear medium sliding frictionless over small bedrock undulations, *J. Glaciol.*, *43*, 71–79.

Gudmundsson, G. H. (1997b), Basal-flow characteristics of a non-linear flow sliding frictionless over strongly undulating bedrock, *J. Glaciol.*, *43*, 80–89.

Hanson, B., R. L. Hooke, and E. M. Grace (1998), Short-term velocity and water-pressure variations down-glacier from a riegel, Storglaciaren, Sweden, *J. Glaciol.*, *44*, 359–367.

Hooke, R. L., P. Calla, P. Holmund, M. Nilsson, and A. Stroeven (1989), A 3 year record of seasonal variations in surface velocity, Storglaciären, Sweden, *J. Glaciol.*, *35*, 235–247.

Hubbard, B., M. J. Siegert, and D. McCarroll (2000), Spectral roughness of glaciated bedrock geomorphic surfaces: implications for glacier sliding, *J. Geophys. Res.*, *105*(B9), 21,295–21,303.

Hutter, K. (1983), *Theoretical Glaciology: Material Science of Ice and the Mechanics of Glaciers and Ice Sheets*, D. Reidel, New York.

Iken, A. (1981), The effect of the subglacial water pressure on the sliding velocity of a glacier in an idealized numerical model, *J. Glaciol.*, *27*, 407–421.

Iken, A., and R. A. Bindschadler (1987), Combined measurements of subglacial water pressure and surface velocity of Findelengletscher, Switzerland: Conclusions about drainage system and sliding mechanism, *J. Glaciol.*, *32*, 101–119.

Iken, A., and M. Truffer (1997), The relationship between subglacial water pressure and velocity of Findelengletscher, Switzerland, during its advance and retreat, *J. Glaciol.*, *43*, 328–338.

Kamb, B. (1970), Sliding motion of glaciers: Theory and observation, *Rev. Geophys.*, *8*(4), 673–728.

Kamb, B. (1987), Glacier surge mechanism based on linked cavity configuration of the basal water conduit system, *J. Geophys. Res.*, *92*(B9), 9083–9100.

Kavanaugh, J. L., and G. K. C. Clarke (2001), Abrupt glacier motion and reorganization of basal shear stress following the establishment of a connected drainage system, *J. Glaciol.*, *47*, 472–480.

Le Meur, E., and C. Vincent (2003), A two-dimensional shallow ice flow model of glacier de Saint Sorlin, France, *J. Glaciol.*, *49*, 527–538.

Lliboutry, L. (1968), General theory of subglacial cavitation and sliding of temperate glaciers, *J. Glaciol.*, *7*, 21–58.

Lliboutry, L. (1979), Local friction laws for glaciers: A critical review and new openings, *J. Glaciol.*, *23*, 67–95.

Lliboutry, L. (1987), Realistic, yet simple bottom boundary conditions for glaciers and ice sheets, *J. Geophys. Res.*, *92*(B9), 9101–9110.

Morland, L. W. (1984), Glacier sliding down an inclined wavy bed, *J. Glaciol.*, *17*, 447–462.

Nye, J. F. (1969), A calculation on the sliding of ice over a wavy surface using a Newtonian viscous approximation, *Proc. R. Soc., Ser. A*, *311*, 445–467.

Nye, J. F. (1970), Glacier sliding without cavitation in a linear viscous approximation, *Proc. R. Soc. London, Ser. A*, *315*, 381–403.

Paterson, W. S. B. (1994), *The Physics of Glaciers*, Pergamon, Oxford.

Pattyn, F. (1996), Numerical modelling of a fast-flowing outlet glacier: Experiments with different basal conditions, *Ann. Glaciol.*, *23*, 237–246.

Pattyn, F. (2002), Transient glacier response with a higher-order numerical ice-flow model, *J. Glaciol.*, *48*, 467–477.

Raymond, C. F. (1971), Flow in a transverse section of Athabasca Glacier, Alberta, *J. Glaciol.*, *10*, 55–84.

Schoof, C. (2002), Basal perturbations under ice streams: Form drag and surface expression, *J. Glaciol.*, *48*, 407–416.

Schoof, C. (2005), The effect of cavitation on glacier sliding, *Proc. R. Soc., Ser. A*, *461*, 609–627.

Van der Veen, C. J. (1987), Longitudinal stresses and basal sliding: A comparative study, in *Proceedings of Workshop on Dynamics of the West Antarctica Ice Sheet*, edited by C. van der Veen and J. Oerlemans, pp. 223–248, D. Reidel, New York.

Weertman, J. (1957), On the sliding of glaciers, *J. Glaciol.*, *3*, 33–38.

D. Cohen, Department of Geological and Atmospheric Sciences, Iowa State University, Ames, IA 50010, USA. (dcohen@ iastate.edu)

O. Gagliardini, Laboratoire de Glaciologie et Géophysique de l'Environnement, CNRS, UJF-Grenoble I, BP 96, F-38402 Saint-Martin d'Hères, France. (gagliar@lgge.obs-grenoble.fr)

P. Råback and T. Zwinger, CSC-Scientific Computing Ltd., P.O. Box 405, Espoo FIN-02101, Finland. (raback@csc.fi; zwinger@csc.fi)